

Chapter 2

The Experiments

2.1 Negative Photoion Spectroscopy

2.1.1 The Synchrotron Radiation Source

Energy must be absorbed by a molecule in order for ion-pair dissociation to occur. *Synchrotron radiation* is ideal for such experiments because it provides a bright, monochromated and tunable energy source across the entire electromagnetic spectrum [1]. Synchrotron radiation sources accelerate electrons at relativistic velocities in a circular orbit using magnets; this takes place in a *storage ring*, tens of metres in diameter. The accelerating charges emit collimated light tangentially to the orbital path. Collected from the storage ring at a *beamline*, the light is optically focused into a monochromator prior to entering the experimental end station. The experiments described in Chaps. 3–6 utilised vacuum ultraviolet (VUV) radiation from beamline 3.1 at the UK Daresbury Synchrotron Radiation Source (SRS).

The Wadsworth monochromator, focal length 1 m, installed on beamline 3.1 is designed to provide the user with a high flux beam, albeit at the expense of wavelength resolution; it does not have an entrance slit limiting the amount of light hitting the *diffraction grating*, as is common in many other designs [2]. A diffraction grating consists of a large number of equally spaced parallel grooves cut into a reflective surface. The angle of the grating relative to the incident light determines which wavelengths will interfere constructively when reflected from the surface. It can be observed from Fig. 2.1 that for constructive interference of light to occur, the difference between distances x_1 and x_2 when divisible by an integer must equal the wavelength, λ ; note that angles i and θ are both measured relative to the same normal reference, one angle taking a positive value, the other a negative value. Distance d represents the spacing between grooves on the surface of the grating. The relationship between the relative position of the grating (with respect to angles i and θ), d and λ can be written as follows:

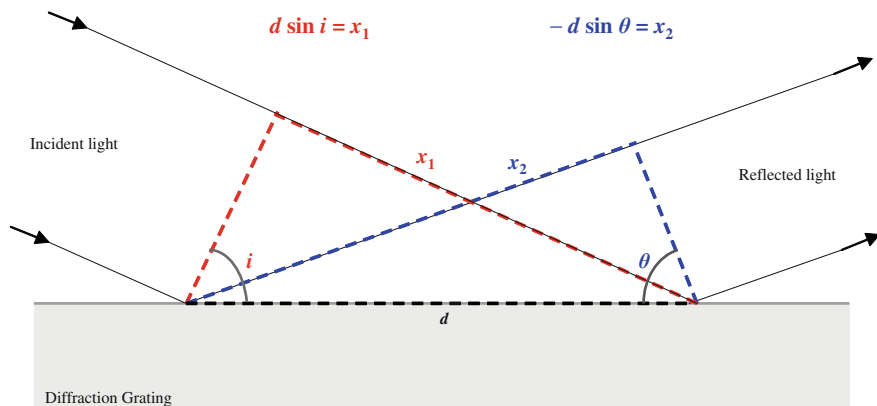


Fig. 2.1 A simple diagram to show how a diffraction grating works. Distances x_1 and x_2 represent the side of a right angle triangle ‘opposite’ to the angles i and θ , respectively. Distance d represents the spacing between grooves on the surface of the grating

$$m\lambda = d(\sin i + \sin \theta) \quad (2.1)$$

where m represents an integer value. When angles i and θ are equal and opposite, all wavelengths of light are constructively reflected and m takes the value of zero: hence the term *zero-order* radiation. During scanning experiments, however, *first-order* radiation is used ($m = 1$). Higher-orders of radiation become a problem when the desired energy of radiation is relatively low, i.e. between 8 and 16 eV. For example, a first-order spectrum at 10 eV may contain unwanted contributions from second-order radiation at 20 eV. In such cases, a lithium fluoride window may be placed in the path of the beam; LiF absorbs all radiation above 11.7 eV, thus eliminating contributions from higher orders.

Two different diffraction gratings are installed within the beamline 3.1 monochromator. The medium energy grating (MEG) is efficient in the range 8–18 eV and the high energy grating (HEG) from 12 to 35 eV. The beam of light reflected from the diffraction grating is directed through a manually controlled slit, known as the *exit slit*, before passing into the experimental endstation. A reduced slit width provides a higher resolution of light for the experiment, but the total flux is reduced; likewise a larger slit provides higher flux for the experiment, but at the expense of resolution.

A few experiments discussed in [Chap. 6](#) used the 5 m focal length McPherson monochromator installed on beamline 3.2 at the SRS. This monochromator provides superior resolution for a given exit slit width compared to 3.1 due to the longer focal length, but the principles of operation are exactly the same as described above.

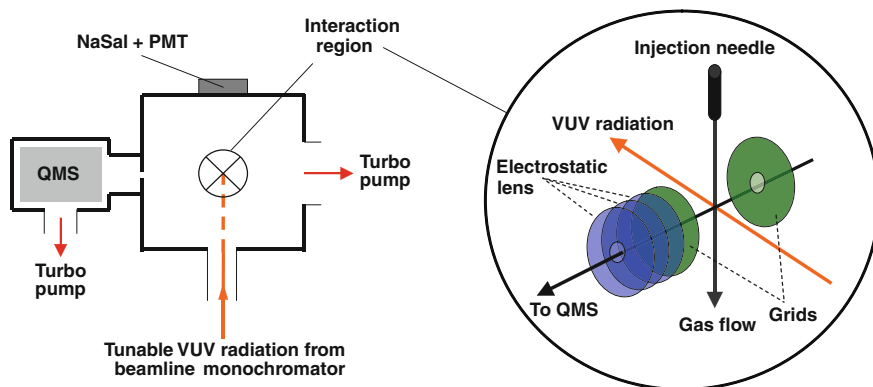


Fig. 2.2 A simple diagram of the experimental endstation used for detecting negative photoions

2.1.2 The Experimental Endstation

A simple diagram showing the main components and setup of the experimental end station is presented in Fig. 2.2, and should be referred to when reading the description below.

A 2 mm diameter, 300 mm long capillary light guide connecting the experimental apparatus to the beamline directs the monochromatised light to the interaction region. The gas under study is injected via a needle generating an effusive directed jet (with no internal cooling) which bisects orthogonally the incident photon beam. The crossing point, which dictates the centre of the interaction region, is positioned in the middle of two grids on the third orthogonal axis. A three-element electrostatic lens for focusing, and into a Hidden Analytical HAL IV triple quadrupole mass spectrometer (QMS) for mass selection. Detection is achieved by a channeltron electron multiplier. Sensitivity is considerably enhanced by differential pumping which reduces the number of free electrons and secondary collisions in the QMS. Spectra in which the monochromator is scanned are flux normalised using a sodium salicylate (NaSal) window and visible photomultiplier tube (PMT) combination, which has a constant response over the energy range of the experiments. The apparatus and QMS, connected via a 1 mm diameter aperture, are pumped separately by turbo pumps which are backed by a common rotary pump, and the base pressure of the apparatus is approximately 10^{-7} mbar. With sample gas running, the typical pressure in the chamber is raised to 10^{-5} mbar. The pressure inside the chamber is measured using an ionisation gauge, the sensitivity of which to the sample gas under study is calibrated in a separate experiment relative to N_2 gas using a capacitance manometer (Dunn 2009 private communication) [3].

Mass spectra are recorded to observe all anions produced from photo absorption of the sample gas by exposure to white light (i.e. zero-order radiation). The mass-to-charge ratio (m/z) of each peak in the mass spectrum is then fixed and the signal

recorded as a function of photon energy, typically over the range 8–35 eV. In addition, for each anion, its signal is recorded at a fixed photon energy (usually the energy of a peak observed in the spectrum) as a function of sample gas pressure over the typical range $(0.5\text{--}5.0) \times 10^{-5}$ mbar. Anions which show a non-linear dependence with pressure cannot be assigned as ion-pair products, and their signal is most likely influenced by secondary processes. Anions which show a linear dependence of signal with pressure can be attributed to ion-pair formation; being a unimolecular process, the rate of formation of ion pairs is expected to obey first-order kinetics. Full details of the pressure dependencies are given in [Chaps. 3–6](#).

2.1.3 The Determination of Absolute Ion-Pair Cross Sections

Anion spectra resulting from ion-pair formation are presented as cross sections, σ , in absolute units of cm^2 . The value of σ at a given photon energy $h\nu$ is calculated as follows:

$$\sigma(h\nu) = k \left(\frac{SM}{f r p} \right) \quad (2.2)$$

where S is the detected signal in counts s^{-1} , M is the relative mass sensitivity of the QMS, f is the relative photon flux (effectively a measure of the grating efficiency), r is the storage ring current, p is the sample gas pressure corrected for ionisation gauge sensitivity and k is a normalisation constant. Normalisation to f , r and p is straight forward, but this is not the case for M . An extensive set of experiments was performed to determine M as a function of m/z , described below in [Sect. 2.1.5](#).

The corrected signal (to M , f , r and p) for F^- from SF_6 is normalised to the known cross section at 14.3 eV of $(7 \pm 2) \times 10^{-21} \text{ cm}^2$ [4]. Likewise, the corrected signal for F^- from CF_4 is normalised to its value at 13.9 eV of $(1.25 \pm 0.25) \times 10^{-21} \text{ cm}^2$ [5]. (It is noted that these known cross section values are not strictly absolute, but are obtained from calibrated measurements of O^- yields from O_2 [6]). Thus, normalisation factors $k(\text{SF}_6)$ and $k(\text{CF}_4)$ are determined. An average of these two k values is then used in Eq. 2.2 to determine cross section values for anions from other gases. In theory, these two values should be the same. In practice, they vary by a factor ranging from 1.2 to 1.7. These measurements were made at every visit to the SRS, and the appropriate average value of k was used.

2.1.4 The Determination of Quantum Yields

The ion-pair cross section from a molecule, calculated as described above in [Sect. 2.1.3](#), can be divided by the *total* photoabsorption cross section for that molecule (absolute values are taken from the literature, where available, and are referenced

where appropriate in [Chaps. 3–6](#)) to provide an ion-pair formation quantum yield, Φ . Thus, the value for Φ represents the probability that the absorption of a photon will lead to ion-pair formation. Individual values for Φ are quoted with the photon energy at which the ion-pair and total photoabsorption cross section values are taken.

2.1.5 Considerations When Detecting Ions with the QMS

All quadrupole mass spectrometers exhibit an element of mass discrimination, with a tendency to transmit heavier ions less efficiently [7]. To correct for this effect the mass factor, M , has been determined by comparing the cation mass spectra of many polyatomic molecules in the QMS, following 70 eV electron impact ionisation, to ‘true’ mass spectra published in the electronic NIST database [8]. The values for M used in [Eq. 2.2](#) are taken from the plot shown in [Fig. 2.3](#). It can be seen that as m/z increases, the detection efficiency of the QMS decreases and a higher M value is required to correct this effect.

The zero-blast effect arises because *all* ions entering the QMS may be transmitted when the applied potentials are set to detect m/z values close to zero [7]. This becomes important when studying hydrogen-containing molecules; the tail of the zero-blast peak in the mass spectrum overlaps with m/z 1. Therefore, H^- spectra can only be trusted where there is no resemblance to other anion spectra recorded from the same molecule. Examples where this has caused problems include H^- detected from CH_3X molecules ($\text{X} = \text{F}, \text{Cl}, \text{Br}$), where the H^- spectra can mimic the X^- spectra [9]. By contrast, H^- detected from CH_4 is an example where this is not an issue because the H^- signal is dominant [10].

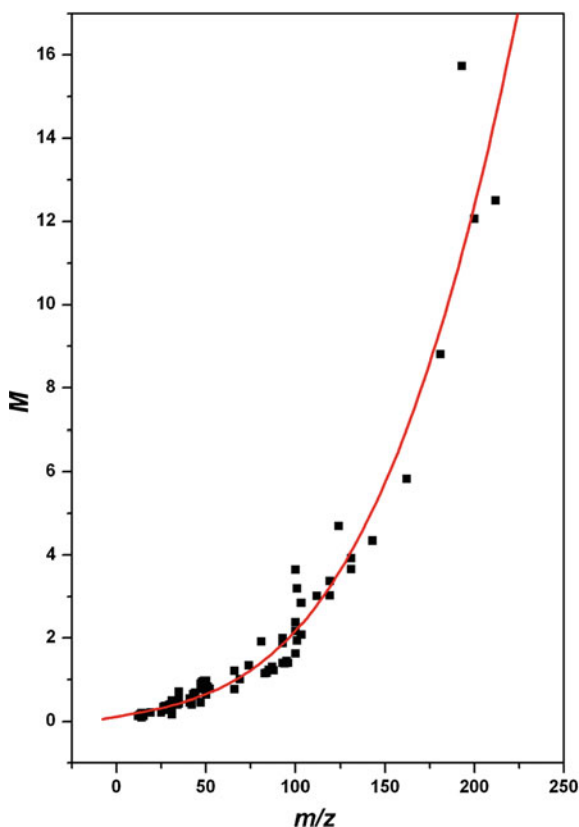
2.2 Ion–Molecule Reactions

2.2.1 The Selected Ion Flow Tube

The Selected Ion Flow Tube (SIFT) is an experimental apparatus used to study gas-phase ion–molecule reactions. An experimental rate coefficient can be measured and the ionic product species for the reaction can be identified. The relative branching ratios (BRs) for the detected products can also be determined. The SIFT technique has been described in detail in several review papers [11–13]. A description of the experiment, and how rate coefficients and BRs are determined, is also presented here.

The SIFT is vacuum sealed, and consists of three distinct sections. First is the ion source, where cations and/or anions are produced from a neutral precursor molecule by electron impact ionisation. Second is the flow tube, where helium

Fig. 2.3 Graph to determine the relative mass sensitivity, M , of the Hidden Analytical HAL IV quadrupole mass spectrometer (QMS) as a function of m/z . Sample gases include CF_4 , SF_6 , SF_5CF_3 , CH_3F , CH_3Cl , CH_3Br , CH_2Cl_2 , CF_2Cl_2 , CFCl_3 , C_2H_4 , C_2H_6 , C_3H_8 , C_2F_4 , C_2F_6 , C_3F_8 , 2- C_4F_8 , c - C_4F_8 , c - C_5F_8 . The mass spectrum of each sample was measured with 70 eV electron impact ionisation, and compared with the NIST spectrum [8]. At each m/z value, the percentage yield from NIST is divided by the percentage yield from the QMS spectrum, and the data are normalised to unity at m/z 69 (i.e. CF_3^+). The squares show data points, the solid line shows the best fit to a third-order polynomial



buffer gas carries the ions downstream to a point where the neutral reactant is injected, and the reaction may occur. Third is the detection region, where the product ions are mass filtered and detected. Figure 2.4 presents a basic schematic of the SIFT, showing how these three sections relate to one another.

The ion source consists of a small closed chamber containing a tungsten filament and a series of electrostatic lenses. A simple cartoon of the ion source, showing the example of selecting C_2F_4^+ ions from C_3F_8 source gas, is presented in Fig. 2.5. When no gas is flowing a diffusion pump, backed by a common rotary pump, achieves a vacuum pressure of ca. 10^{-6} mbar. During operation, a neutral source gas is introduced into the chamber such that a relatively high pressure is maintained, ca. 10^{-4} mbar. Molecules from the source gas are ionised by 70 eV electrons; the filament emits electrons which are subsequently accelerated by an applied potential difference. This process may produce many different cation and anion species. For example, C_2F_6 may be used to produce the ions F^+ , CF^+ , CF_2^+ , CF_3^+ , F^- and CF_3^- . The reactant ions used in this work and their corresponding source gases are listed in Table 2.1. For the ions to enter the flow tube they must first pass through the electrostatic lenses and then through a quadrupole mass filter.

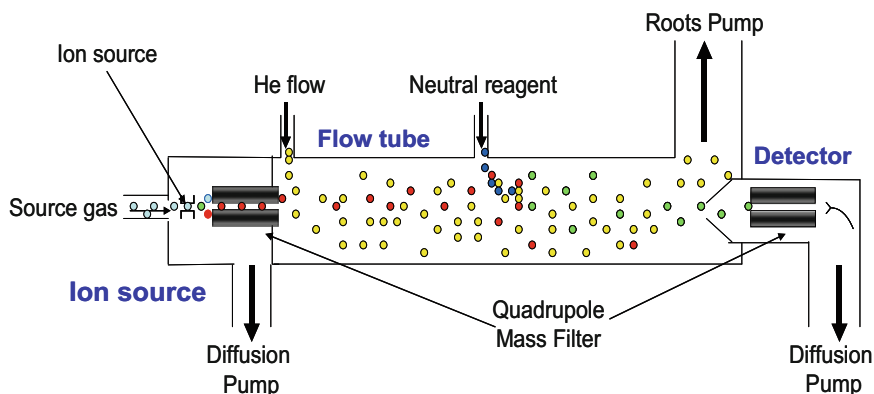


Fig. 2.4 A basic schematic of the Selected Ion Flow Tube apparatus. The *red* circles represent the ions generated in the ion source, the *yellow* circles represent the helium buffer gas, the *blue* circles represent the neutral reactant gas, and the *green* circles represent the product species

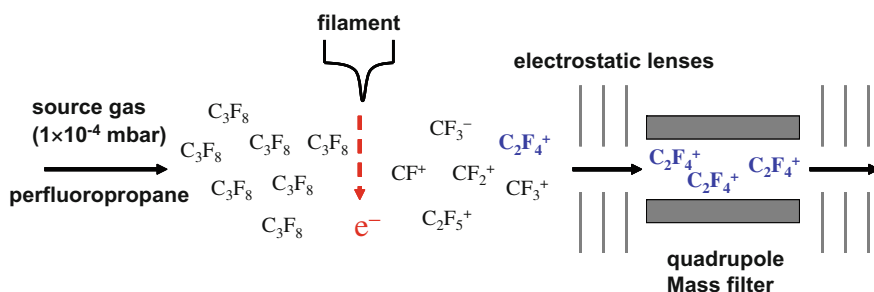


Fig. 2.5 A simple cartoon of the ion source in the Selected Ion Flow Tube, showing the example of selecting C_2F_4^+ ions using perfluoropropane source gas

Table 2.1 Source gases used to produce reactant cations and anions in the ion source

Ion	Source gas	Process
CF^+	$\text{CF}_4/\text{C}_2\text{F}_6/\text{C}_3\text{F}_8$	Single electron impact
CF_2^+	$\text{CF}_4/\text{C}_2\text{F}_6/\text{C}_3\text{F}_8$	Single electron impact
CF_3^+	$\text{CF}_4/\text{C}_2\text{F}_6/\text{C}_3\text{F}_8$	Single electron impact
C_2F_4^+	C_3F_8	Single electron impact
O_2^-	$\text{N}_2 + \text{O}_2$ mixture	Collisionally stabilised electron attachment
O^-	N_2O	Dissociative electron attachment
OH^-	$\text{N}_2\text{O} + \text{CH}_4$ mixture	Dissociative electron attachment forming O^- , followed by H abstraction from CH_4
F^-	C_2F_6	Dissociative electron attachment
CF_3^-	C_2F_6	Dissociative electron attachment

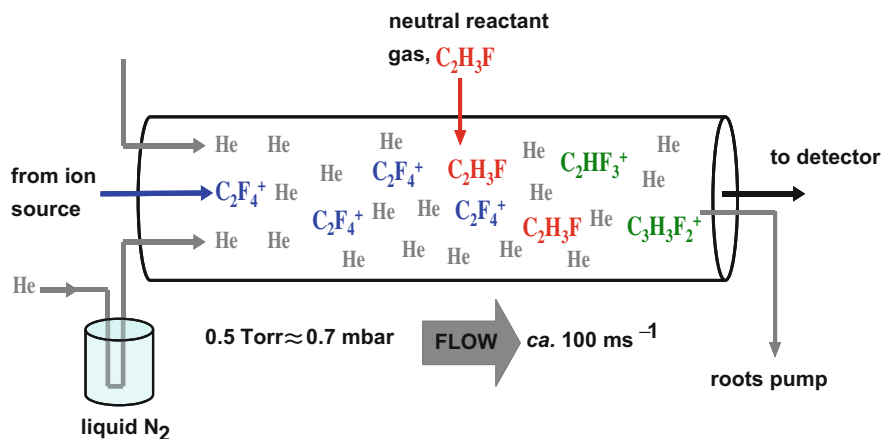


Fig. 2.6 A simple cartoon showing the flow tube part of the Selected Ion Flow Tube apparatus. The example of the reaction between C_2F_4^+ with $\text{C}_2\text{H}_3\text{F}$ is used. The helium buffer gas is shown in grey, the reactant ion in blue, the reactant neutral in red, and the product ions in green

The quadrupole can be set to a desired mass-to-charge ratio (m/z) value with one atomic mass unit (a.m.u) resolution, such that only the desired reactant ion is selected. The ion signal is then maximised by monitoring the signal at the detection region (discussed below) by tuning the electrostatic lenses. The lens settings in the ion source are significantly different for positive or negative ions. For example, if the signal is maximised to transmit CF_3^+ ions (detection region set to positive mode) then CF_3^- anions produced will be repelled by the lens system, and not reach the mass filter. In addition, altering the pressure in the ion source can have an effect on the resultant ion signal.

The selected ions enter the flow tube along with helium (99.997% purity) buffer gas. The helium gas is passed through liquid nitrogen to increase its purity, and injected into the flow tube in a way which is designed to minimise back streaming of helium into the ion source [11]. The flow tube is 1 m in length and 8 cm in diameter. During operation it is filled with 0.5 Torr of buffer gas, which is drawn downstream at a velocity of $\text{ca. } 100 \text{ m s}^{-1}$ by an Edwards EH 2600 roots pump, backed by an Edwards E1M176 rotary pump. The conditions inside the flow tube are thermal, and the measurements in this work are all reported at 298 K. Any excited ions produced in the ion source are expected to be collisionally cooled by the buffer gas. At a known distance along the flow tube the neutral reactant gas is introduced. A simple cartoon of the flow tube is shown in Fig. 2.6, using the example of C_2F_4^+ ions reacting with $\text{C}_2\text{H}_3\text{F}$. All species, including helium, reactants and products, will then continue down the flow tube towards the detection region of the apparatus.

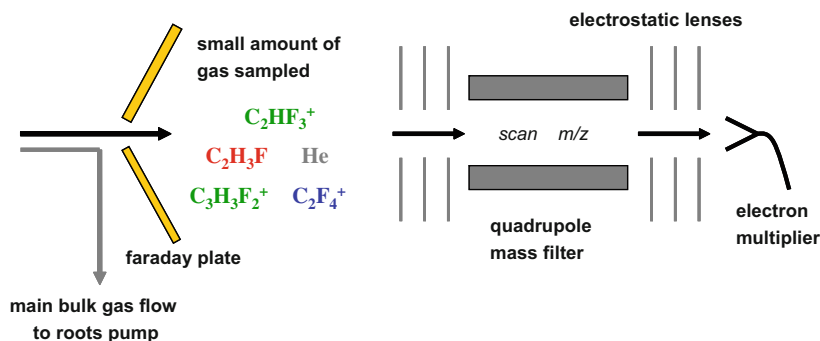


Fig. 2.7 A simple cartoon showing the detection region of the Selected Ion Flow Tube apparatus showing the example of reacting C_2F_4^+ with $\text{C}_2\text{H}_3\text{F}$

A simple cartoon of the detection region of the SIFT apparatus is shown in Fig. 2.7. At the end of the flow tube is a cone shaped end plate, with a 1 mm diameter hole at the centre. It is this orifice which samples the gas from the flow tube, and is the only connection to the detection region. The main bulk gas flow is drawn away by the roots pump as shown in Figs. 2.6 and 2.7. The detection region is differentially pumped by a diffusion pump backed by a common rotary pump; the base pressure in this region is ca. 10^{-6} mbar (compared to 0.7 mbar in the flow tube) and during operation the small amount of sampled gas through the end plate raises the pressure to ca. 10^{-5} mbar. The end plate not only samples the gas, but also acts as a Faraday plate. It has a floating voltage applied (being electrically isolated from the rest of the system), and the current produced is proportional to the number of ions hitting it.

Measurement of the current is therefore useful to tune the ion signal from the ion source, as discussed above. In addition, when reacting anions in the SIFT, a drop in the ion current can indicate a reaction is ejecting electrons; an electron is much lighter than an atomic or molecular anion, and so hits the wall of the flow tube rather than reaching the Faraday plate, which results in the total ion current decreasing. Ions are drawn into the quadrupole mass filter by electrostatic lenses, and then towards a channeltron electron multiplier which records the resultant ion signal. The ion signal is recorded as a function of m/z , and a mass spectrum is obtained.

2.2.2 The Determination of the Reaction Rate Coefficient

In the reactions performed in the SIFT the concentration of the reactant neutral molecule is much greater than the concentration of the reactant ion. This allows pseudo first-order kinetics to be applied, and if we consider the generic

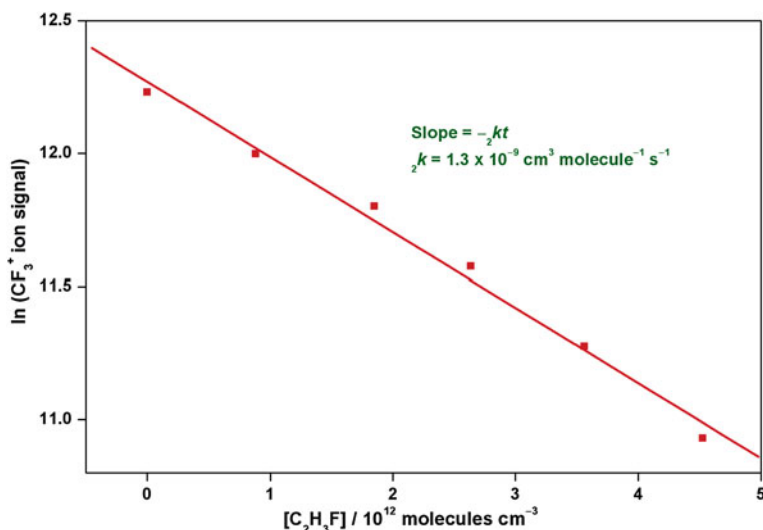


Fig. 2.8 A rate coefficient plot for the reaction between CF_3^+ and C_2H_3F . Computer software fits the data points to a straight line. The reaction time in s, t , is also calculated by the data analysis software, and a value for the bimolecular rate coefficient, ${}_2k$, is given in units of $\text{cm}^3 \text{ molecule}^{-1} \text{ s}^{-1}$

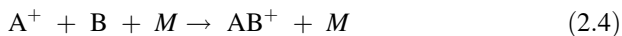
ion–molecule reaction as being $A^+ + B$, then the integrated rate equation can be given as:

$$\frac{\ln[A^+]_{rel}}{[B]} = -{}_2kt \quad (2.3)$$

where $[A^+]_{rel}$ is the relative ion concentration (this is simply the ion count recorded by the mass spectrometer), $[B]$ is the neutral reactant concentration (the absolute concentration of B (in molecules cm^{-3}) measured during the experiment as described in Appendix IV), ${}_2k$ is the bimolecular rate coefficient, and t is the reaction time. Equation 2.3 shows that the gradient of a linear plot of $\ln[A^+]_{rel}$ vs. $[B]$ will be equal to $-{}_2kt$. An example of such a plot, for the reaction between CF_3^+ and C_2H_3F , is shown in Fig. 2.8.

The reaction time cannot be measured independently, but can be calculated by dividing the reaction length, z , by the ion flow velocity, v_i . The reaction length is a known value defined by the point along the flow tube where the neutral reactant enters, and Smith and Adams have given a detailed account of how v_i can be measured [11]. An experimental value for ${}_2k$ (in $\text{cm}^3 \text{ molecule}^{-1} \text{ s}^{-1}$) can therefore be calculated. Such measurements are repeated several times until a consistent result is achieved, and the estimated uncertainty in the value obtained is ca. $\pm 20\%$. Experimentally-measured bimolecular rate coefficients are referred to as k_{exp} .

In some reactions performed in the SIFT, an association product is observed. These reactions are pressure dependent due to the involvement of a third body, M , and so the rate equation includes a third-order rate coefficient, ${}_3k$:



$$rate = {}_3k [M][A^+][B] \quad (2.5)$$

where the square brackets represent concentrations of the respective species in molecule cm^{-3} , ${}_3k$ has units of $\text{cm}^6 \text{ molecule}^{-2} \text{ s}^{-1}$, and the *rate* has units of molecule $\text{cm}^{-3} \text{ s}^{-1}$. In the SIFT M is most likely to be helium, and in Eq. 2.5 $[M]$ can be considered constant. A bimolecular rate coefficient is still measured for association reactions, as described above and shown in Fig. 2.8, but in these cases it is a *pseudo* second-order rate coefficient, ${}_2k'$. This value can be related to ${}_3k$ if the concentration of M is known:

$${}_2k' = {}_3k [M] \quad (2.6)$$

In association reactions discussed in this report the value for ${}_2k'$ is quoted because it can then be compared with other bimolecular rate coefficients. However, the rate coefficient of an association reaction is only valid at a given pressure of M , and so where ${}_2k'$ is quoted the pressure of helium recorded at the time is also given. Knowing the pressure of M allows $[M]$ to be calculated in much the same way as $[B]$ is calculated, as described in Appendix IV.

2.2.3 The Determination of the Product Branching Ratios

Product branching ratios (BRs) are recorded in much the same way as the rate coefficient is measured, however, rather than the reactant ion signal, it is the *product* ion signals which are recorded as a function of neutral reactant concentration.

The individual product ion counts are converted into a percentage of the total product ion counts, and plotted using data analysis software. A line through the data points is added using a polynomial fit, and the %BR values are taken by extrapolating to zero neutral reactant concentration, which aims to eliminate any contributions from secondary reactions. An example of such a plot is provided in Fig. 2.9 for the reaction between CF_3^+ and $\text{C}_2\text{H}_3\text{F}$. The mass spectrum recorded for this reaction showed product peaks at m/z 27 (C_2H_3^+), 47 ($\text{C}_2\text{H}_4\text{F}^+$), 51 (CHF_2^+) and 53 ($\text{CH}_2\text{F}_2\text{H}^+$). For the products at m/z 47 and 53 a BR of 0% is determined, indicating these are secondary products. The primary products for this reaction are m/z 27 (C_2H_3^+) and m/z 51 (CHF_2^+) with BRs of 75 and 25%, respectively.

The reported BR values have a $\pm 20\%$ uncertainty. This error is an estimate based on the variation in experimentally detected relative ion signals and the

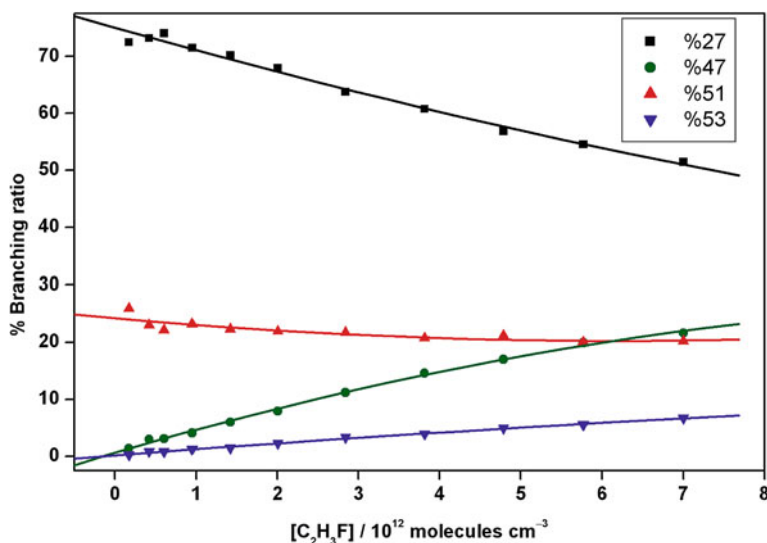


Fig. 2.9 A branching ratio (BR) plot for the products detected from the reaction between CF_3^+ and $\text{C}_2\text{H}_3\text{F}$. The products are indicated by their m/z values shown in the *top right* corner of the graph. At zero $\text{C}_2\text{H}_3\text{F}$ concentration the BRs are 75 and 25% for the primary products C_2H_3^+ (m/z 27 in black) and CHF_2^+ (m/z 51 in red), respectively. The plots corresponding to m/z 47 (green) and m/z 53 (blue) show a BR of 0%, indicating they are secondary products

polynomial data fitting; it is noteworthy that $\pm 20\%$ is a modest estimate for the example data provided in Fig. 2.9.

References

1. Hulbert SL, Williams GP (2000) In: Samson JA, Ederer DL (eds) Vacuum ultraviolet spectroscopy. Academic, London
2. Howle CR, Ali S, Tuckett RP, Shaw DA, West JB (2005) Nucl Instrum Methods Phys Res Sect B 237:656
3. Simpson MJ, Tuckett RP (2011) Int Rev Phys Chem 30:197
4. Mitsuke K, Suzuki S, Imamura T, Koyano I (1990) J Chem Phys 93:8717
5. Mitsuke K, Suzuki S, Imamura T, Koyano I (1991) J Chem Phys 95:2398
6. Dehmer PM, Chupka WA (1975) J Chem Phys 62:4525
7. Dawson PH (1995) Quadrupole mass spectrometry and its applications. American Institute of Physics, NY
8. National Institute of Standards and Technology website (<http://webbook.nist.gov/chemistry/>)
9. Rogers NJ, Simpson MJ, Tuckett RP, Dunn KF, Latimer CJ (2010) PCCP 12:10971
10. Rogers NJ, Simpson MJ, Tuckett RP, Dunn KF, Latimer CJ (2010) Mol Phys 108:895
11. Smith D, Adams N (1988) Adv At Mo Phys 24:1
12. Graul ST, Squires RR (1988) Mass Spectrom Rev 7:263
13. Bohme DK (2000) Int J Mass Spectrom 200:97

Two Studies in Gas-Phase Ion Spectroscopy
Vacuum-Ultraviolet Negative Photoion Spectroscopy
and Ion-Molecule Reaction Kinetics

Simpson, M.J.

2012, XIV, 162 p., Hardcover

ISBN: 978-3-642-23128-5